Available online at www.sciencedirect.com
ScienceDirect
Comput. Methods Appl. Mech. Engrg. 393 (2022) 114786
Computer methods in applied mechanics and engineering
www.elsevier.com/locate/cma

An adaptive peridynamics material point method for dynamic fracture problem☆

Zhixin Zeng[a], Heng Zhang[a], Xiong Zhang[a,*], Yan Liu[a], Zhen Chen[b]

[a] School of Aerospace Engineering, Tsinghua University, Beijing 100084, PR China
[b] Department of Civil and Environment Engineering, University of Missouri, Columbia, MO, 65211, USA

Received 11 December 2021; received in revised form 17 February 2022; accepted 17 February 2022
Available online xxxx

Abstract

An adaptive peridynamics material point method (APDMPM) is proposed for modeling dynamic fracture problems to fully take advantage of both the peridynamics (PD) and material point method (MPM). The PD is used to model the crack region of a continuum, while the MPM is used to model the remaining regions of the continuum. A hand-shake region is employed to transfer the interaction between the PD and MPM particles. The simulation region is initially discretized by MPM particles, which will be adaptively converted to PD particles based on their stress condition or connect relation to make the PD sub-region fit the damage area automatically. Several numerical examples, including spallation of Hopkinson bar, plate with a pre-existing crack and plate with a circular cutout under velocity boundary conditions, are studied to verify the proposed method. The numerical results show that the APDMPM can successfully predict the initiation and propagation of cracks without explicitly tracking crack surface, meanwhile improve the calculation efficiency and accuracy of the rest of the region.

Keywords: Peridynamics; Material point method; Dynamic fracture

1. Introduction

The dynamic fracture problem is fundamental in the fracture mechanics and the focus of many engineering problems, and its scientific analysis and reasonable prediction have attracted much attentions since 19th century. Inglis and Griffith [1] made contributions to the early development of fracture mechanic theory, and Irwin extended the Griffith's [1] model by developing the energy release rate concept. However, the complexity of the fracture problems greatly increases the difficulty of theoretical analysis, making the numerical method especially important in the study of fracture problems. In order to model crack growth, various numerical models have been proposed. The so-called element erosion technique is commonly employed in the finite element method (FEM) for material failure modeling, but it suffers difficulties in mass and energy conservation. The finite difference method (FDM) [2] was considered by Chen and Wilkins for fracture problems analysis. The extended finite element method (XFEM) was proposed by Belytschko and his collaborators [3] with the method of unity principle partition for cracks modeling.

☆ Supported by the National Natural Science Foundation of China (12172192).
* Corresponding author.
E-mail address: xzhang@tsinghua.edu.cn (X. Zhang).

https://doi.org/10.1016/j.cma.2022.114786
0045-7825/

Cohesive zone method (CZM) [4] was presented by embedding the cohesive zone at the edges or facets of the original FEM mesh. However, in above continuum theory based models, the complex damage models and branching criteria are needed.

Thus, many kinds of meshfree methods have been proposed aiming at modeling fracture problems. Carpiteri et al. [5] presented an augment Lagrangian element-free (ALEF) approach based on the construction of shape functions with a moving least-squares approximation. Krysl and Belytschko [6] presented the Element-Free Galerkin method (EFG) for modeling 3D dynamically propagating cracks of elastic materials. Rao and Rahman [7] proposed an interaction integral to calculate stress-intensity factors (SIFs) for mixed-mode fracture analysis with EFG, which can also be implemented in conjunction with FEM. A simplified meshfree method, called as cracking-particle method, was presented by Belytschko [8] for arbitrary evolving cracks modeling, in which the crack was presented by a discontinuous enrichment and the explicit crack presentation is not required. Rabczuk et al. [9] further developed a three-dimensional (3D) cracking-particle method, in which the additional unknowns in the variational formulation to capture the displacement discontinuity were not needed. Instead, the particles, where cracking is detected, are split into two particles lying on opposite sides of the crack. Many efforts have been made in material point method (MPM) to simulate crack problems. Nairn [10] proposed a material point method with crack (CRAMP), in which a crack with multi-velocity fields was simulated. Wang et al. [11] used an irregular mesh to simulate two-dimensional (2D) mixed mode crack and introduced the surfaces of the crack by allowing the placement of two node sets along the crack line. Chen et al. [12] simulated several crack problems approximately by using the collection of failure points and developed a failure criterion based on a bifurcation analysis. Yang et al. [13] simulated the fragmentation with MPM based on Gurson model and random failure. Yang et al. [14] presented a combined elastoplasticity and decohesion model with MPM for the crack problem, in which the decohesion modeling is improved by making the failure mode adjustable, and the critical normal and tangential decohesion strengths with the tensile and shear peak strengths are utilized. Liang et al. [15,16] proposed a generalized interpolation material point method (GIMP) with enriched shape function (EMPM/EGIMP) for modeling crack problems, which utilizes fracture parameters of the crack tip such as the energy release rate and stress intensity factors. Soga et al. [17] used Mohr–Coulomb, Cam-Clay and other derivatives to simulate the shear bands in the landslide cases. Cheon and Kim [18] proposed an adaptive MPM coupled with phase-field fracture model with the refinement of background grid based on the amount of material damage. In above studies, some achievements have been made in modeling crack problems, but various limitations still exist. First, the location and normal vector of the crack surface need to be explicitly described in these methods, and additional relations are required to relate the initiation of cracks with their growth velocity and direction, which makes it difficult to simulate cracking initiation problems.

In recent years, peridynamics (PD) [19–21] has attracted wide interests in fracture problems. PD is based on non-local governing equations, and shows great flexibility in modeling dynamic fractures because the internal force of peridynamic particle relies on the interaction between particles. The crack growth happens naturally without explicitly tracking crack surface, and cracking initiation and propagation can be well simulated with the use of PD. There are three types of PD formulations: the bond-based PD [20], the ordinary state-based PD [22] and the non-ordinary state-based PD [23,24]. Silling [19–21] presented the bond-based PD as the bond acting like independent springs, where the internal force between two particles is only related to their relative position. To overcome the restriction of Poisson's ratio in bond-based PD, two state-based PD formulations [22–24] have been proposed, in which the internal force between two particles depends not only on their relative position, but also on the deformation statement of their horizons. Various works have been done based on these three PD formulations. Hu et al. [25] propose a computational method for a homogenized PD description of fiber-reinforced composites. Madenci et al. [26] presented a PD least squares minimization (LSM) approach to construct explicit analytical expressions in integral form for PD approximation of a field variable and its derivatives. Silling et al. [27] introduced a PD Eulerian model equipped with a Mie–Gruneisen equation of state. Zhang and Qiao [28] proposed a coupled PD model combining both strength and fracture energy condition for open-hole failure analysis. Madenci et al. [29] presented the ordinary state-based PD constitutive relations for plastic deformation based on the Von Mises yield criteria with isotopic hardening. He et al. [30,31] proposed a coupled PD-CZM method, in which a nonlocal CZM is established in the frame of PD through introducing an objective and precise damage model based on the energy equivalence. However, due to its non-local governing equations, PD has poor accuracy and computational efficiency when dealing with material boundaries and large deformation problems.

Because of its unique capability in fracture simulation, PD has been combined with other methods with local governing equations such as FEM [32] and FDM [33]. However, several limitations will be raised in the combined PD/FEM procedure. Firstly, a complicated interfacial treatment must be implemented between the PD sub-region and the FEM sub-region [32]. Secondly, FEM has difficulty in simulating extreme deformation problems due to element distortion [34,35]. Thirdly, it is required that PD sub-region covers the whole fracture area which limits the use of PD/FEM procedure in complicated fracture problems. The combined PD/FDM procedure [33] also suffers from the limitation of complicated interfacial treatment and computation area division. Lubineau et al. [36] developed a morphing strategy which divides the strain energy into non local part and local continuum part to adaptively couple non-local to local continuum mechanics. In this method, the important feature is the definition of the morphing functions, which relies on energy equivalence. However, this method also has the aforementioned first two limitations.

MPM [37,38] is an extension of the particle-in-cell (PIC) method [39]. In the MPM scheme [38], a continuum body is discretized into a set of particles which carry all the physical data moving through a predefined Eulerian background grid. The momentum equation is first solved on the background grid, and then the solution is mapped to the particles to update their state variables. The deformed background grid is discarded at the end of every time step, and a new regular mesh is used in the next time step. The MPM combines the Lagrangian description and Eulerian description, which makes MPM has relatively natural contact algorithm and robust capability in simulating large deformation problems [37,38]. However, the MPM still has limitations in tracking crack surface and crack initiation problems. Because both PD and MPM are particle methods which simulate dynamic process with particles by explicit time integral, the combination of PD and MPM is very natural and is able to overcome the aforementioned limitations in the combined PD/FEM procedure. Therefore, it is desirable to study the combined PD/MPM procedure for solving crack problems with large deformation. Zeng et al. [40] proposed a combined peridynamics/generalized interpolation material point method (GIMP) via volume modification for simulating transient responses, and Lyu [41] presented a novel integral-based MPM. However, existing combination of PD and other methods requires a pre-partition of simulation sub-region to guarantee the PD sub-region covers the whole fracture area. To overcome these drawbacks, an adaptive peridynamics material point method (APDMPM) is proposed in this paper. The simulation region is initially discretized by MPM particles, which will be adaptively converted to PD particles based on their stress condition or connect relation to make the PD sub-region fit the damage area automatically.

The remaining part of this paper is organized as follows. Sections 2 and 3 briefly review the MPM and PD theories, respectively. Section 4 proposes a coupling scheme for PD and MPM, and develops an adaptive algorithm to convert MPM particles to PD particles adaptively. Two types of conversion criteria are proposed, which are based on the connection factor and principal stress of the particles, respectively. Section 5 presents several numerical examples to verify and validate the proposed method, and Section 6 draws concluding remarks.

2. Material point method

In the MPM [37,38], a continuum body is discretized into a set of particles which carry all the physical data (velocity, momentum, density, etc.). Particles move through the Eulerian background grid during simulation, as shown in Fig. 1. Therefore, the density of the continuum body can be written as

$$\rho(\mathbf{x}) = \sum_{p=1}^{n_p} m_p \delta(\mathbf{x} - \mathbf{x}_p), \tag{1}$$

where ρ is the current mass density, $\mathbf{x}$ is the position vector, m_p and $\mathbf{x_p}$ are the mass and position vector of particle p, respectively. The weak form of the momentum equation and traction boundary condition in updated Lagrangian form can be expressed as

$$\int_\Omega \rho \ddot{u}_i \delta \ddot{u}_i \mathrm{d}V + \int_\Omega \rho \sigma_{ij}^s \delta u_{i,j} \mathrm{d}V - \int_\Omega \rho b_i \delta u_i \mathrm{d}V - \int_{\Gamma_t} \rho t_i^s \delta u_i \mathrm{d}A = 0. \tag{2}$$

In Eq. (2), the subscripts i and j indicate the components of the spatial variables following the Einstein convention, Ω is the material domain, Γ_t denotes the traction boundary, u_i denotes the displacement, $\sigma_{ij}^s = \sigma_{ij}/\rho$ is the specific stress, b_i and t_i^s are the specific body and traction forces, respectively. Substituting Eq. (1) into Eq. (2),

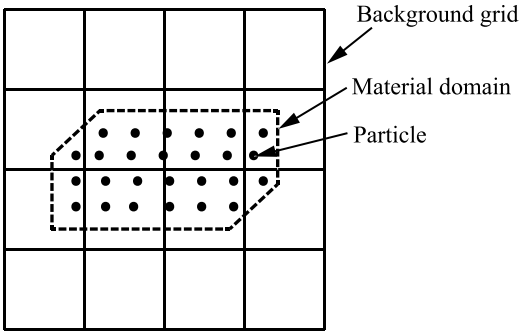

Fig. 1. MPM discretization.

the discretized equation can be expressed as:

$$\sum_{p=1}^{n_p} m_p \ddot{u}_{ip} \delta u_{ip} + \sum_{p=1}^{n_p} m_p \sigma_{ijp}^s \delta u_{ip,j} - \sum_{p=1}^{n_p} m_p b_{ip} \delta u_{ip} - \sum_{p=1}^{n_p} m_p \bar{t}_{ip}^s \delta u_{ip} h^{-1} = 0, \tag{3}$$

where the subscript p denotes the variables associated with particle p, n_p is the number of MPM particles, h is the thickness of the fictitious layer used to convert the surface integral on the traction boundary Γ_{t} into a volume integral.

The position and displacement field of particles can be approximated on the background grid as

$$x_{ip} = \sum_I N_{Ip} x_{iI} \tag{4}$$

$$u_{ip} = \sum_I N_{Ip} u_{iI} \tag{5}$$

where the subscript I denotes the variables associated with the grid node I, N_{Ip} denotes the shape function of grid node I evaluated at particle p. Substituting Eq. (5) into Eq. (3) leads to

$$\dot{p}_{iI} = f_{iI}^{\mathrm{int}} + f_{iI}^{\mathrm{ext}} \qquad x_I \notin \Gamma_u \tag{6}$$

where Γ_u denotes the prescribed displacement boundary of the material domain,

$$p_{iI} = m_I \dot{u}_{iI} \tag{7}$$

is the grid nodal momentum,

$$m_I = \sum_{p=1}^{n_p} m_p N_{Ip} \tag{8}$$

is the grid nodal mass,

$$f_{iI}^{\mathrm{int}} = -\sum_{p=1}^{n_p} N_{Ip,j} \sigma_{ijp} \frac{m_p}{\rho_p} \tag{9}$$

and

$$f_{iI}^{\mathrm{ext}} = \sum_{p=1}^{n_p} m_p N_{Ip} b_{ip} + \sum_{p=1}^{n_p} N_{Ip} \bar{t}_{ip}^s h^{-1} \frac{m_p}{\rho_p} \tag{10}$$

are the internal and external grid nodal force, respectively.

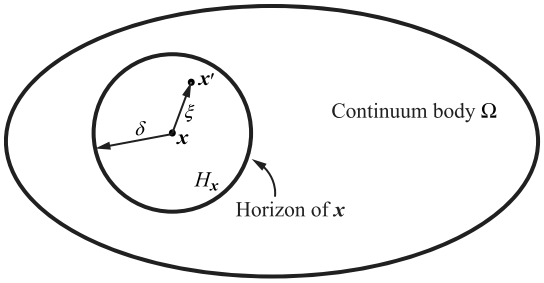

Fig. 2. Internal force calculation of peridynamics.

3. Peridynamics

In the peridynamics theory [19–21], a non-local method is used to calculate the internal force. As shown in Fig. 2, the equation of motion of PD point is given as

$$\int_{H_x} \boldsymbol{f}(\boldsymbol{x}, \boldsymbol{x}', \boldsymbol{u}, \boldsymbol{u}')\mathrm{d}V_{\boldsymbol{x}'} + \rho\boldsymbol{b} - \rho\ddot{\boldsymbol{u}} = 0 \tag{11}$$

where $\boldsymbol{f}$ is the pairwise force function, ρ denotes the mass density, $\boldsymbol{u}$ denotes the displacement field, $H_{\boldsymbol{x}} = \left\{\boldsymbol{x}' | (\boldsymbol{x}' - \boldsymbol{x})^2 < \delta^2\right\}$ denotes the horizon of $\boldsymbol{x}$, δ is the horizon size, $\boldsymbol{b}$ is the density of external body force. The relative position vector $\boldsymbol{\xi}$ in the reference configuration is expressed as

$$\boldsymbol{\xi} = \boldsymbol{x}' - \boldsymbol{x}, \tag{12}$$

and the relative displacement vector η can be written as

$$\boldsymbol{\eta} = \boldsymbol{u}' - \boldsymbol{u}. \tag{13}$$

To assure the conservation of linear momentum, the pairwise force function is required to satisfy

$$\boldsymbol{f}(-\boldsymbol{\xi}, -\boldsymbol{\eta}) = -\boldsymbol{f}(\boldsymbol{\xi}, \boldsymbol{\eta}) \tag{14}$$

Therefore, the pairwise force function can be expressed as

$$\boldsymbol{f}(\boldsymbol{\xi}, \boldsymbol{\eta}) = \begin{cases} 0 & if\ \|\boldsymbol{\xi}\| > \delta \\ f(\boldsymbol{\xi}, \boldsymbol{\eta})\frac{\boldsymbol{\xi}+\boldsymbol{\eta}}{\|\boldsymbol{\xi}+\boldsymbol{\eta}\|} & if\ \|\boldsymbol{\xi}\| \leq \delta. \end{cases} \tag{15}$$

The bond stretch s of two particles can be written as

$$s(\boldsymbol{\xi}, \boldsymbol{\eta}, t) = \frac{\|\boldsymbol{\xi} + \boldsymbol{\eta}\| - \|\boldsymbol{\xi}\|}{\|\boldsymbol{\xi}\|}. \tag{16}$$

For elastic materials, the pairwise force function can be written as

$$f(\boldsymbol{\xi}, \boldsymbol{\eta}) = cs(\boldsymbol{\xi}, \boldsymbol{\eta}, t)\mu(\boldsymbol{\xi}, \boldsymbol{\eta}, t), \tag{17}$$

where c is the micro-modulus, and μ is the scalar function for the bond failure. The micro-modulus c can be calculated by the equation of strain energy density in the classical elasticity theory. For two-dimensional (2D) and three-dimensional (3D) cases, the micro-modulus c is defined as

$$c = \begin{cases} 12k/\pi h\delta^3 & 2D \\ 18k/\pi\delta^4 & 3D, \end{cases} \tag{18}$$

where k is the bulk modulus of the material, and h is the thickness of 2D domain. The scalar function μ is defined as

$$\mu(\boldsymbol{\xi}, \boldsymbol{\eta}, t) = \begin{cases} 1 & s(\boldsymbol{\xi}, \boldsymbol{\eta}, t') < s_c\ \ \forall t' < t \\ 0 & \text{otherwise}, \end{cases} \tag{19}$$

where s_c is the critical stretch of the bond which can be calculated by the critical energy release rate G_c of the materials. For different space dimensions, the critical stretch is defined by

$$s_c = \begin{cases} \sqrt{\dfrac{5G_c}{2b\pi\delta^6}} & \text{2D} \\ \sqrt{\dfrac{G_c}{bh\delta^5}} & \text{3D} \end{cases} \tag{20}$$

In peridynamic numerical model, integrating the motion equation Eq. (11) in the current configuration Ω with body density Eq. (1), the discretized form of the motion equation can be written as

$$m_{\boldsymbol{x}}\boldsymbol{u}(\boldsymbol{x},t) = \sum_{\boldsymbol{x}'\in H_{\boldsymbol{x}}} \boldsymbol{f}(\boldsymbol{\xi},\boldsymbol{\eta})V_{\boldsymbol{x}'}V_{\boldsymbol{x}} + \boldsymbol{b}(\boldsymbol{x},t)V_{\boldsymbol{x}} \tag{21}$$

where $V_{\boldsymbol{x}}$ and $V_{\boldsymbol{x}'}$ are the volumes of particles $\boldsymbol{x}$ and $\boldsymbol{x}'$, respectively. To measure the failure of particle $\boldsymbol{x}_k$, the scalar parameter of particle damage is defined as

$$\phi(\boldsymbol{x}_k,t) = 1 - \frac{\sum_{i=1}^{n_k}\mu(\boldsymbol{x}_k,\boldsymbol{x}_i,t)V_{\boldsymbol{x}_i}}{\sum_{i=1}^{n_k}V_{\boldsymbol{x}_i}} \tag{22}$$

where n_k is the total number of particles in the neighborhood of the particle $\boldsymbol{x}_k$.

4. Adaptive peridynamics material point method

To develop the adaptive peridynamics material point method(APDMPM), two main issues must be considered. The first one is coupling of PD and MPM particles. In Liu's Work [32], a special interface element is adopted to bridge the FEM subregion and PD subregion, and the interface element is embedded with several PD particles to calculate the coupling force. Because both PD and MPM are meshless methods with discrete particles, the calculation of interaction force between MPM and PD particles is simple and natural, by the similar calculation scheme used to calculate the interaction force between PD particles. The coupling scheme of PD and MPM is presented in Section 4.1. The second challenge is the adaptive conversion of MPM particles to PD particles to gain the simulation efficiency from MPM and the discontinuities modeling ability from PD. Therefore, the MPM subregion should cover the most of the continuum body to improve the simulation efficiency, meanwhile the PD subregion must cover the failure part of the continuum to guarantee the simulation accuracy of crack growth. To satisfy the above requirements, two MPM particle conversion criteria are presented in Section 4.2. The one of them is based on the connection relationship of PD particles and MPM particles for crack growth, and the other one is based on the stress state of MPM particles for crack initiation.

4.1. Coupling of peridynamics and material point method

To couple PD with MPM, a hand-shake subregion is employed, as shown in Fig. 3. A continuum body is divided into three subregions: the MPM subregion, PD subregion and hand-shake subregion. The particles located in the MPM subregion, PD subregion and hand-shake subregion are named as MPM particles, PD particles and hand-shake particles, respectively for short. The physical data of the MPM particles are updated by the method described in Section 2, while the physical data of the PD particles are updated by the method described in Section 3.

The hand-shake particles are those particles covered by the horizon of a PD particle, as shown in Fig. 4. The hand-shake particles play two roles. Firstly, they serve as MPM particles whose physical data are updated by the solution of the background grid as described in Section 2, in which the interaction forces from PD particles are taken into account. Secondly, they serve as virtual PD particles to determine the interaction force between PD particles and hand-shake particles. The interaction force between PD particle m and hand-shake particle p can be written as

$$\boldsymbol{f}_{mp}^{\mathrm{PD}} = c\frac{\boldsymbol{\xi}+\boldsymbol{\eta}}{\|\boldsymbol{\xi}+\boldsymbol{\eta}\|}s(\boldsymbol{\xi},\boldsymbol{\eta},t)\mu(\boldsymbol{\xi},\boldsymbol{\eta},t)V_mV_p \tag{23}$$

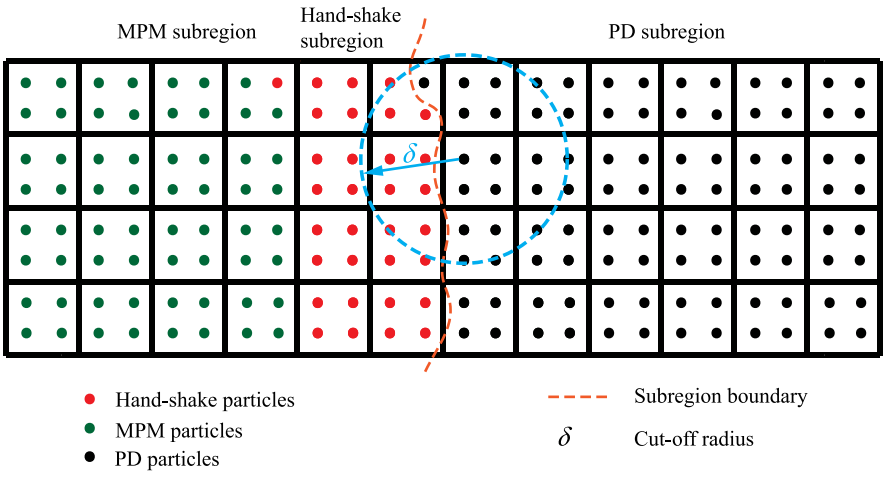

Fig. 3. Coupling between peridynamics and material point method.

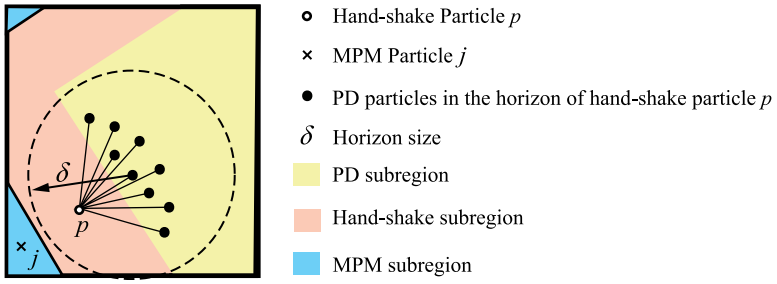

Fig. 4. Calculation of coupling force f_{mp}^{PD}.

The interaction force $\boldsymbol{f}_{mp}^{\mathrm{PD}}$ will be simultaneously applied on the PD particle m and hand-shake particle p. Summing up interaction forces from all PD particles whose horizon cover the hand-shake particle p, an extra external force of the hand-shake particle p, is given as

$$\boldsymbol{f}_{p}^{\mathrm{PD}} = -\sum_{m=1}^{n_p^{\mathrm{PD}}} \boldsymbol{f}_{mp}^{\mathrm{PD}} \tag{24}$$

where n_p^{PD} is the number of PD particles whose horizons cover the hand-shake particle p. Therefore, the background grid nodal external force Eq. (10) can be replaced by

$$f_{iI}^{\mathrm{ext}} = \sum_{p=1}^{n^{\mathrm{MH}}} m_p N_{Ip} b_{ip} + \sum_{p=1}^{n^{\mathrm{MH}}} N_{Ip} \bar{t}_{ip}^{s} h^{-1} \frac{m_p}{\rho_p} + \sum_{p=1}^{n^{\mathrm{MH}}} f_{ip}^{\mathrm{PD}} N_{Ip}, \tag{25}$$

where n^{MH} is the total number of MPM particles and hand-shake particles. Note that $\boldsymbol{f}_{p}^{\mathrm{PD}} = 0$ for all MPM particles because they are not covered by any PD particles, as particle j shown in Fig. 4. Therefore, we can unify the calculation of the external force of background grid with Eq. (25). As shown in the next section, it is unnecessary to distinguish the MPM particles and hand-shake particles in simulation process by using a connection factor. Therefore, we will term all these particles as MPM particles.

4.2. Adaptive conversion of MPM particles

To gain the simulation efficiency from MPM and the capacity of discontinuity simulation from PD, an adaptive conversion algorithm is proposed in this work. A continuum body is initially discretized by a set of particles

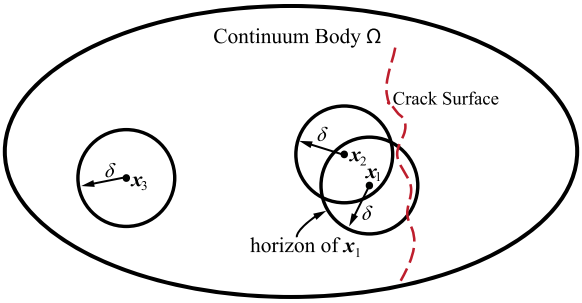

Fig. 5. Particle division with pre-existing crack.

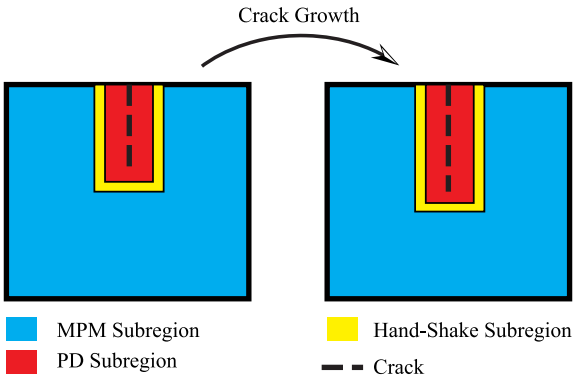

Fig. 6. Region division of adaptive algorithm.

which carry all the physical data. For problems with pre-existing cracks, these particles are classified as MPM particles, hand-shake particles and PD particles in the initial configuration. As shown in Fig. 5, the particle $\boldsymbol{x}_1$ will be classified as a PD particle, because the initial crack surface crosses its horizon. Particles like $\boldsymbol{x}_2$ which are covered by the horizon of a PD particle but whose horizons are not crossed by a crack surface will be classified as hand-shake particles. Particles like $\boldsymbol{x}_3$ which are far away from crack surface will be classified as MPM particles. After the classification of particles, the domain is partitioned into the MPM subregion, PD subregion and hand-shake subregion as shown in Fig. 6. The PD subregion will only cover the area where the crack is located, and the area near the crack tips which is expected to grow. During the crack growth, the MPM sub-region will be adaptively converted to PD sub-region, as shown in Fig. 6.

To establish the APDMPM, two MPM particle conversion criteria are proposed. The first conversion criterion is based on the connection relationship and the break of the bond between MPM particles and PD particles. To develop this criterion, a connection factor in initial configuration K_{pq}^0 between particle $\boldsymbol{x}_p$ and $\boldsymbol{x}_q$ is defined as

$$K_{pq}^0 = \begin{cases} \frac{c}{|x_p - x_q|} V_p V_q & x_p \in H_q \\ 0 & \text{otherwise} \end{cases} \tag{26}$$

where the subscripts p and q denote all particles, including PD particles, MPM particles and hand-shake particles. Therefore, the connection factor should be calculated between all particle pairs. For problems with pre-existing cracks, the connection factor should be corrected by

$$K_{pq}^1 = a_{pq} K_{pq}^0 \tag{27}$$

where $a_{pq} = 0$ if the bond between particle x_p and x_q cross the pre-existing crack, otherwise a_{pq} is equal to 1. Then, the particles can be classified as MPM particles and PD particles based on their corrected connection factor

by

$$\boldsymbol{x}_p \in \begin{cases} S_{\mathrm{MPM}} & \dfrac{\sum_q K_{pq}^1}{\sum_q K_{pq}^0} = 1 \\ S_{\mathrm{PD}} & \dfrac{\sum_q K_{pq}^1}{\sum_q K_{pq}^0} < 1 \end{cases} \tag{28}$$

With the connection factor K_{pq}^k (k refers to the time step), the interaction force between PD particle p and particle q in its horizon at time step k can be written as

$$\boldsymbol{f}_{\boldsymbol{pq}} = K_{pq}^k(\|\boldsymbol{\xi}+\boldsymbol{\eta}\| - \|\boldsymbol{\xi}\|)\frac{\boldsymbol{\xi}+\boldsymbol{\eta}}{\|\boldsymbol{\xi}+\boldsymbol{\eta}\|} \tag{29}$$

Therefore, we can simply update the connection factor K_{pq}^k in every time step to calculate the internal force of PD particles and the interaction force between PD particles and MPM particles. To adaptively convert the MPM particles during crack growth, the connection factor K_{pq}^k needs to be updated in every time step. Because the PD subregion needs to cover all the failure parts of the continuum, all the MPM particles in hand shake region with a broken bond need to be converted into PD particles after the position update. Therefore in every time step, the connection factor K_{pq}^k can be updated based on the updated displacement by

$$K_{pq}^{k+1} = \begin{cases} K_{pq}^k & s_{pq}(t) < s_c \\ 0 & s_{pq}(t) > s_c \end{cases} \tag{30}$$

where s_{pq} is the bond stretch between particle x_p and x_q, and s_c is defined in Eq. (20).

Note that only the connection factors between PD particles or PD particle and MPM particle need to be update. The connection factor between MPM particles is not related to the calculation of interaction force, so it does not need to be updated until one of the MPM particles is converted to a PD particle. After the update of the connection factor K_{pq}^{k+1}, the adaptive conversion MPM particles can be performed by the following criterion. For any MPM particle x_p, if

$$\frac{\sum_j K_{pq}^{k+1}}{\sum_j K_{pq}^0} < 1 \quad x_p \in S_{\mathrm{MPM}}, \tag{31}$$

then x_i will be converted to a PD particle in the next time step. The connection factor criterion implies that all the MPM particles in shake-hand region with a broken bond will be converted to PD particles. With Eq. (31), the conversion of sub-regions will be carried out adaptively with the growth of cracks, and it can guarantee that all the failed parts are simulated by PD. As presented in Eq. (29), the connection factor is also used in the calculation of the internal force of PD particles, and the interaction force between PD particles and MPM particles. Therefore, this conversion criterion introduces only a little extra computational cost.

As discussed above, the connection factor criterion can resolve the MPM particle conversion of pre-existing crack growth problem, but it is difficult to simulate the crack initiation problem because only particles in the hand-shake subregion could be converted to PD particles in every time step. To model crack initiation in MPM subregion, a criterion related to the state of stress is proposed for MPM particles, which can be expressed as $f(\sigma_{ij}) > 0$. The specific expression of $f(\sigma_{ij})$ depends on the failure form of the material. In this study, the maximum principal stress criterion is employed, namely,

$$f(\sigma_{ij}) = \sigma_1 - \alpha\sigma_{\max} > 0 \tag{32}$$

where σ_1 is the maximal principal stress of the MPM particles, $\alpha < 1$ is a positive constant, and $\sigma_{\max}$ is the strength of extension. Any MPM particle x_p which satisfies Eq. (32) will be converted to a PD particle in the next time step. This stress criterion generates new PD subregion in the continuum, which can be applied to simulate the initiation of a crack.

4.3. Numerical procedure of the APDMPM

Based on the adaptive conversion criteria proposed above, the simulation process of the APDMPM can be summarized as follows. Firstly, the following steps are performed prior to the first time step:

(a). Discretize the continuum body by a set of particles. Each particle carries its all physical properties.

(b). Calculate the initial connection factor K_{pq}^0 between all particle pairs based on the particle position in the initial configuration with Eq. (26).

(c). Correct the initial connection factor K_{pq}^0 for pre-existing crack problems based on the crossing status of crack path and bonds with Eq. (27).

(d). Classify the particles into MPM particles and PD particles with corrected connection factor by Eq. (28).

For each time step, the following steps are performed:

(1) Reform the regular background mesh and reconstruct the mass and momentum of background grid nodes from MPM particles by

$$m_I^k = \sum_{p=1}^{n^{\mathrm{MPM}}} m_p N_{Ip}^k \tag{33}$$

$$p_{iI}^{k-1/2} = \sum_{p=1}^{n^{\mathrm{MPM}}} m_p v_{ip}^{k-1/2} N_{Ip}^k \tag{34}$$

For fixed boundary, apply the essential boundary condition $p_{iI}^{k-1/2} = 0$.

(2) Calculate the internal force of PD particles with the connection factor K_{ij}^k by Eq. (35),

$$\boldsymbol{f}_p^k = \sum_{p=1}^{n^p} \boldsymbol{f}_{pq}^{\boldsymbol{k}} = \sum_{p=1}^{n^p} K_{pq}^k (\|\boldsymbol{\xi}+\boldsymbol{\eta}\| - \|\boldsymbol{\xi}\|) \frac{\boldsymbol{\xi}+\boldsymbol{\eta}}{\|\boldsymbol{\xi}+\boldsymbol{\eta}\|} \quad \boldsymbol{x}_p \in S_{\mathrm{PD}} \tag{35}$$

where n^p is the total number of all particles. While calculating the internal force of PD particles, the interaction force between MPM particles and PD particles is also calculated. If particle q is a MPM particle, the interaction force $\boldsymbol{f}_{pq}$ needs to be added to its external force $\boldsymbol{f}_q^{\mathrm{PD}}$. The interaction force can be written as

$$\boldsymbol{f}_q^{\mathrm{PD,k}} = -\sum_{p=1}^{n^{\mathrm{PD}}} \boldsymbol{f}_{pq}^{\boldsymbol{k}} = -\sum_{p=1}^{n^{\mathrm{PD}}} K_{pq}^k (\|\boldsymbol{\xi}+\boldsymbol{\eta}\| - \|\boldsymbol{\xi}\|) \frac{\boldsymbol{\xi}+\boldsymbol{\eta}}{\|\boldsymbol{\xi}+\boldsymbol{\eta}\|} \quad \boldsymbol{x}_q \in S_{\mathrm{MPM}} \tag{36}$$

where n^{PD} denotes the total number of all PD particles.

(3) Calculate the background grid nodal forces by

$$f_{iI}^{\mathrm{int},k} = -\sum_{p=1}^{n^{\mathrm{MPM}}} N_{Ip,j}^k \sigma_{ijp}^k \frac{m_p}{\rho_p} \tag{37}$$

$$f_{iI}^{\mathrm{ext},k} = \sum_{p=1}^{n^{\mathrm{MPM}}} m_p N_{Ip}^k b_{ip}^k + \sum_{p=1}^{n^{\mathrm{MPM}}} N_{Ip}^k \bar{t}_{ip}^k h^{-1} \frac{m_p}{\rho_p^k} + \sum_{p=1}^{n^{\mathrm{MPM}}} f_{ip}^{\mathrm{PD,k}} N_{Ip}^k, \tag{38}$$

$$f_{iI}^k = f_{iI}^{\mathrm{int},k} + f_{iI}^{\mathrm{ext},k} \tag{39}$$

and update the grid nodal momentum by

$$p_{iI}^{k+1/2} = p_{iI}^{k-1/2} + f_{iI}^k \Delta t^k \tag{40}$$

(4) Map the updated grid nodal velocity and acceleration to MPM particles to update their velocity and displacement by

$$x_{ip}^{k+1} = x_{ip}^k + \Delta t^{k+1/2} \sum_{I=1}^{8} \frac{p_{iI}^{k+1/2} N_{Ip}^k}{m_I^k} \tag{41}$$

$$v_{ip}^{k+1/2} = v_{ip}^{k-1/2} + \Delta t^k \sum_{I=1}^{8} \frac{f_{iI}^k N_{Ip}^k}{m_I^k} \tag{42}$$

and update the velocity and displacement of PD particles by

$$\boldsymbol{v}_i^{k+1/2} = \boldsymbol{v}_i^{k-1/2} + \Delta t^k \frac{\boldsymbol{f}_i^k}{m_i} \tag{43}$$

$$\boldsymbol{x}_i^{k+1} = \boldsymbol{x}_{ip}^k + \Delta t^{k+1/2} \boldsymbol{v}_i^{k+1/2} \tag{44}$$

(5) Update the connection factor K_{pq}^k between PD particles or PD particle and MPM particle based on the updated displacement by Eq. (30).

(6) Reconstruct the grid momentum from updated MPM particles by

$$p_{iI}^{k+1/2} = \sum_{p=1}^{n_{MPM}} m_p v_{ip}^{k+1/2} N_{Ip}^k \tag{45}$$

and apply the essential boundary condition. Calculate the updated grid node velocity by

$$v_{iI}^{k+1/2} = \frac{p_{iI}^{k+1/2}}{m_i^n} \tag{46}$$

(7) Calculate MPM particles' incremental strain and incremental vorticity by

$$\Delta\varepsilon_{ijp}^{k+1/2} = \Delta t^{k+1/2} \sum_{I=1}^{8} \frac{1}{2} (N_{Ip,j}^k v_{iI}^{k+1/2} + N_{Ip,i}^k v_{jI}^{k+1/2}) \tag{47}$$

$$\Delta\Omega_{ijp}^{k+1/2} = \Delta t^{k+1/2} \sum_{I=1}^{8} \frac{1}{2} (N_{Ip,j}^k v_{iI}^{k+1/2} - N_{Ip,i}^k v_{jI}^{k+1/2}) \tag{48}$$

and update MPM particles' stress by a constitutive model, and density by

$$\rho_p^{k+1} = \frac{\rho_p^n}{(1 + \Delta\varepsilon_{iip}^{k+1/2})} \tag{49}$$

(8) Perform the adaptive conversion of MPM particles. Convert MPM particle $\boldsymbol{x}_i$ to a PD particle in the next time step if it satisfies Eq. (31) or Eq. (32).

The flow chart of the APDMPM is shown in Fig. 7.

5. Numerical examples

5.1. Spallation of Hopkinson bar

In this section, the planar spallation with a hypothetical material in 1D condition is studied. As shown in Fig. 8, an impactor strikes on a bar at velocity of $v_0 = 30$ m/s. Both the impactor and the bar are assumed to be elastic with a Young's modulus $E = 10000$ Pa, mass density $\rho = 1$ kg/m^3, and $\sigma_{\max} = 3000$ Pa. The lengths of the impactor and the bar are $L_1 = 0.03$ m and $L_2 = 0.07$ m respectively, and the width of the impactor and the bar is $D = 0.001$ m. In this problem, the elastic wave analysis is performed of a spall plane at $x = 0.04$ m from the left end of the plate. The conversion criterion Eq. (32) is employed with $\alpha = 0.95$ to model the crack initiation process in spallation, and the bond critical stretch is chosen as $s_c = 0.3$.

The bar is discretized into a set of particles with spacing of $\Delta = 1$ mm and horizon of $\delta = 3.015\Delta$. The side length of the background grid cell for MPM is chosen as 2 mm, and the time step Δt is set as 5.0×10^{-7} s. The evolution of the particle type is plotted in Fig. 9(a), where hollow circles denote the MPM particles while crosses denote the PD particles. The damage value $\phi(\boldsymbol{x}_k, t)$ (see Eq. (22)) distributions along the plate at different time are shown in Fig. 9(b), which shows that the location of the spallation plane agrees with theoretical predicted location $x = 0.04$ m from the left end of the bar, and the spallation time also matches the theoretical predicted time. Fig. 10 shows the displacement after the spallation. Because the material of the impactor and the bar are the same, the length of the spallation part (right part) of the bar is equal to the length of the impactor $L_1 = 0.03$ m. Therefore, the impactor and the left part of the bar will be approximately static after the impact, and the spallation part will move with a velocity slightly below $v_0 = 30$ m/s due to the elastic deformation, which all agree well with the theoretical prediction. In this numerical example, we use MPM particles to model the impact between the impactor and the bar with background grids, which overcomes the difficulty of the contact between PD particles.

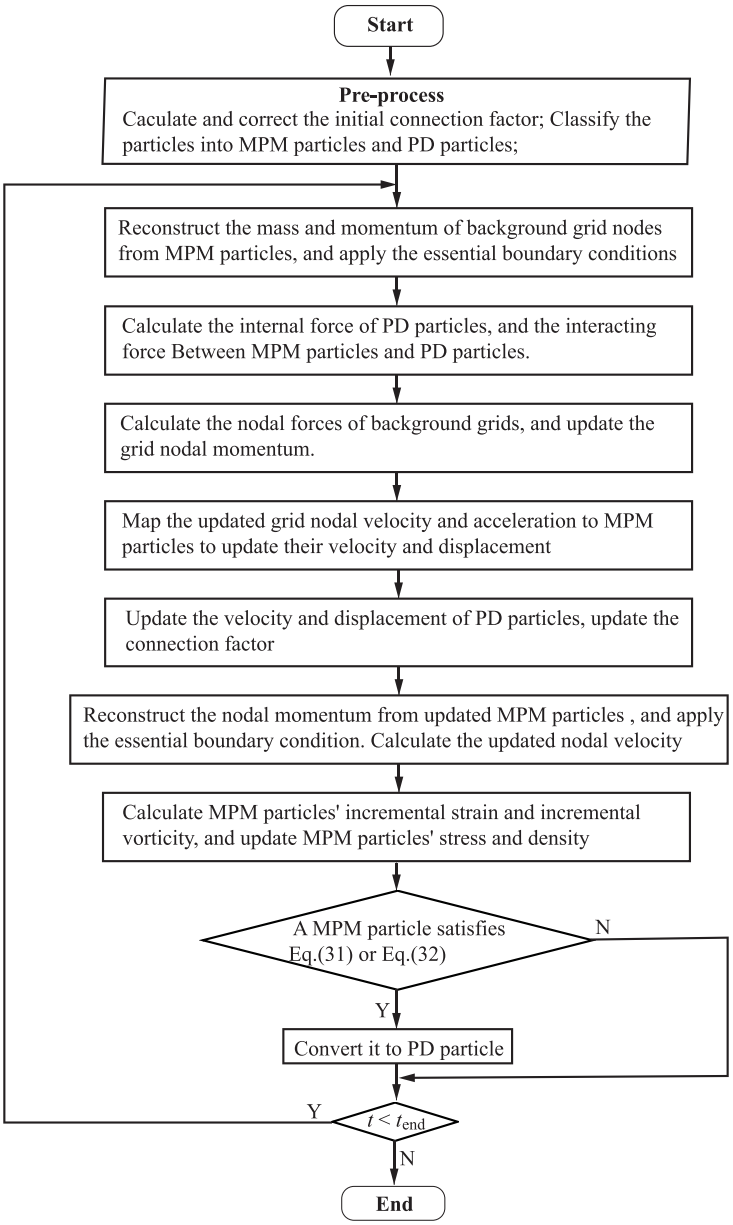

Fig. 7. Flow chart of the APDMPM.

Fig. 8. Hopkinson bar.

5.2. *Plate with a pre-existing crack under velocity boundary conditions*

In this section, the crack growth is simulated. As shown in Fig. 11(a), an isotropic plate with a center pre-existing crack is subjected to a velocity condition on its horizontal edges. The material density, Young's modulus

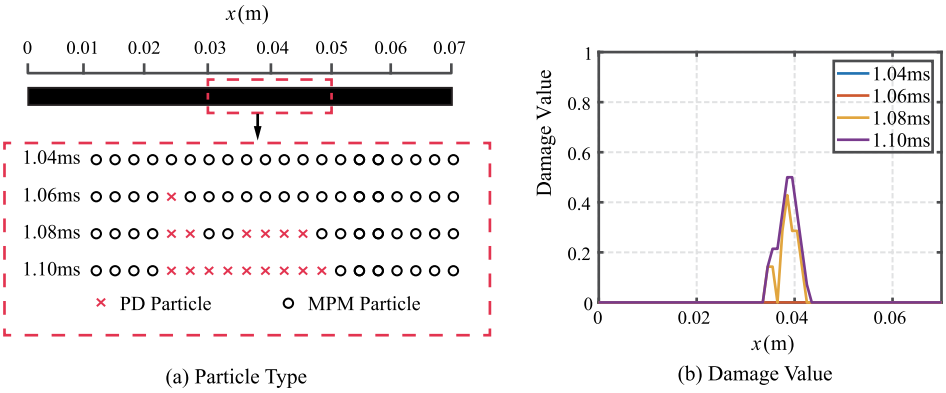

(a) Particle Type (b) Damage Value

Fig. 9. Points type and damage value at different time.

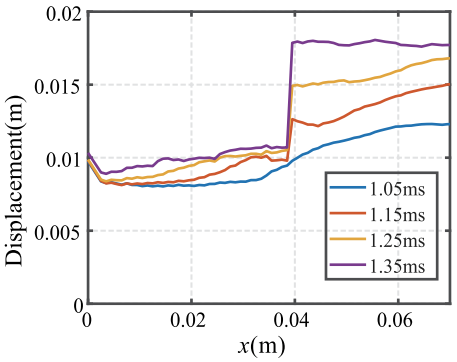

Fig. 10. Displacement of the bar at different time.

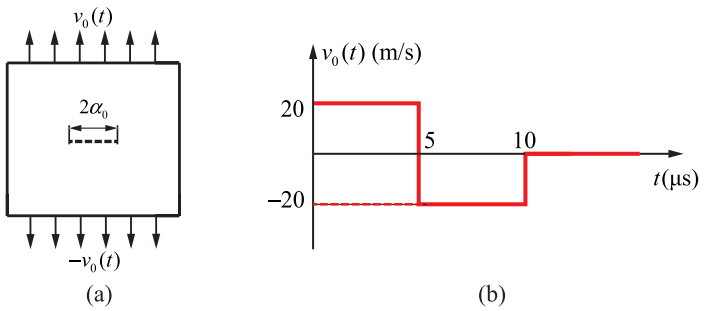

(a) (b)

Fig. 11. Plate with a pre-existing crack under velocity boundary conditions.

and Poisson's ratios are 8000 kg/m^3, 192 Gpa and 1/3, respectively. The initial length of the crack $2a_0 = 10$ mm, the length and thickness of the square plate are 50 mm and 0.1 mm, respectively. The critical stretch is taken as $s_c = 0.02$, and the velocity boundary conditions are applied as shown in Fig. 11(b).

The square plate is discretized into a set of particles with mesh size of $\Delta = 0.5$ mm and $\delta = 3.015\Delta$. The side length of the background grid cell for MPM is chosen as $l_d = 2\Delta = 1$ mm, and the time step $\Delta t = 1.2 \times 10^{-8}$ s which satisfies the stability conditions of PD [21] and MPM [42]. The particles are initially classified into MPM particles and PD particles based on Eq. (28), as shown in Fig. 12(a), where the particles near the pre-existing crack are classified as PD particles to simulate the discontinuity.

The evolution of dynamic crack growth is observed when the stretch wave arrives the crack tips. The classifications of particles at different time are shown in Fig. 12. As the crack growth, MPM particles are adaptively

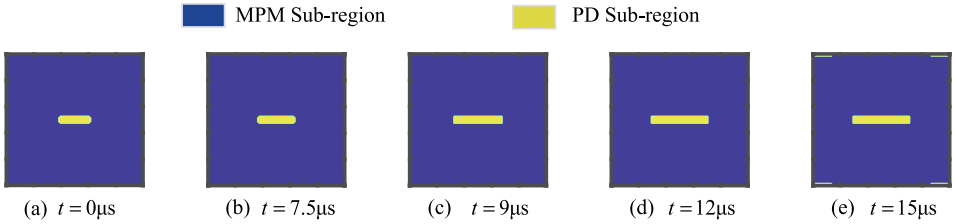

Fig. 12. Simulation sub-region of different time.

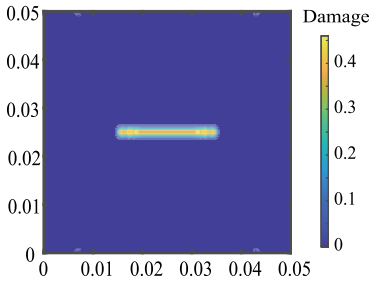

Fig. 13. Damage value at $t = 15$ μs.

converted to PD particles to model crack. As shown in Fig. 12(e), some MPM particles near the boundary in the tensile are converted to PD particles when the stress wave arrives at the boundary. However, as the damage value of the plate at $t = 15$ μs is shown in Fig. 13, the bonds of these PD points have rarely broken which agrees with Silling's results [21]. The crack tip position at any time is defined to be the maximum value of all nodes whose $\phi_i > 0.3$, where ϕ_i denotes the nodal value of the damage defined in Eq. (22). Therefore, the crack growth distance as a function of time is shown in Fig. 14(b). The differential of the curve plotted in Fig. 14(b) gives the maximum predicted crack growth speed of about 1300 m/s, which is less than the material Rayleigh wave speed of $v_r = 2800$ m/s, and it is located within the theoretical limitations [43] for steady mode-I fracture. The simulation results of crack growth distance agrees with the Silling's PD results [21]. The proportion of PD particles as a function of time is plotted in Fig. 14(a), which shows four stages: (1) $0 \sim 6$ μs: the number of PD particles remains unchanged; (2) $6 \sim 10$ μs: the proportion of PD particles raises to 2.5% with the growth of the crack; (3) $10 \sim 12.8$ μs: the number of PD particles remains unchanged; (4) $12.8 \sim 15$ μs: the proportion of PD particles raises to 3.5%, because the stress wave reaches the boundary and the MPM particles are in tensile and converted to PD particles based on the stress criterion Eq. (32).

To test the convergence of the APDMPM, the calculation is carried out with all parameters held constant, but four different values of particle spacing $\Delta = 1.0$ mm, 0.625 mm, 0.5 mm, 0.3125 mm. The resulting predictions for crack growth distance are shown in Fig. 15, and the damage value of the plate at $t = 15$ μs is shown in Fig. 16. The results show that variations in the predicted crack initiation time, arrest time, total growth distance, and velocity, are on the order of the variations in grid spacing. This demonstrates the linear convergence of the predicted dynamic fracture behavior as Δ is reduced in a practical sense. And the weight of the damage area also decrease as Δ is reduced as shown in Fig. 16.

5.3. Plate with a circular cutout under velocity boundary condition

In this section, a mixed mode crack initiation and propagation problem is simulated. As shown in Fig. 17, the pre-existing crack of the square plate in Section 5.2 is replaced by a circular cutout with a diameter of $D = 10$ mm. The velocity boundary condition along its horizontal edges is given as

$$v_0(x, \pm L/2, t) = 10 \text{ m/s} \qquad t > 0 \tag{50}$$

The material properties, plate geometry and the material parameters are the same as those used in Section 5.2 except for the plate thickness $h = 0.5$ mm. Due to the lack of preset crack, Eq. (28) cannot be employed to classify

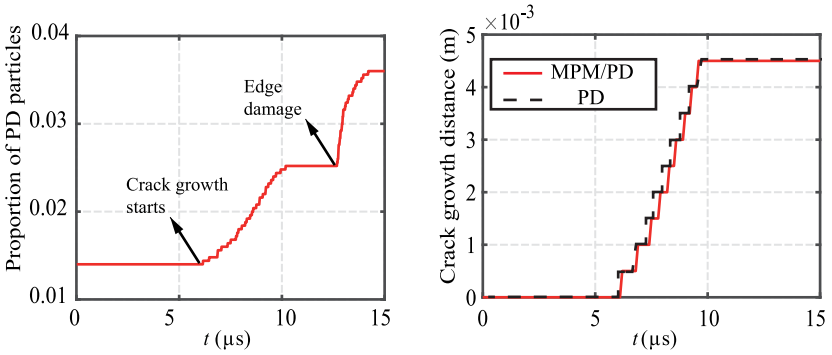

Fig. 14. Proportion of PD particles and crack growth distance.

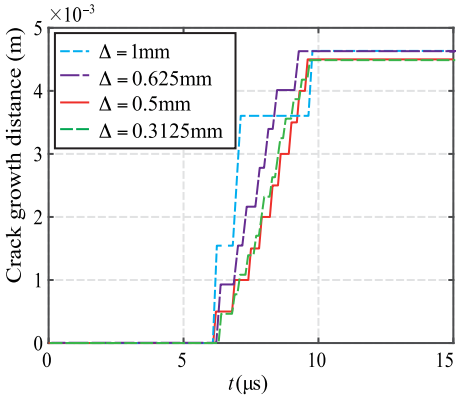

Fig. 15. Crack growth distance with different discretization size.

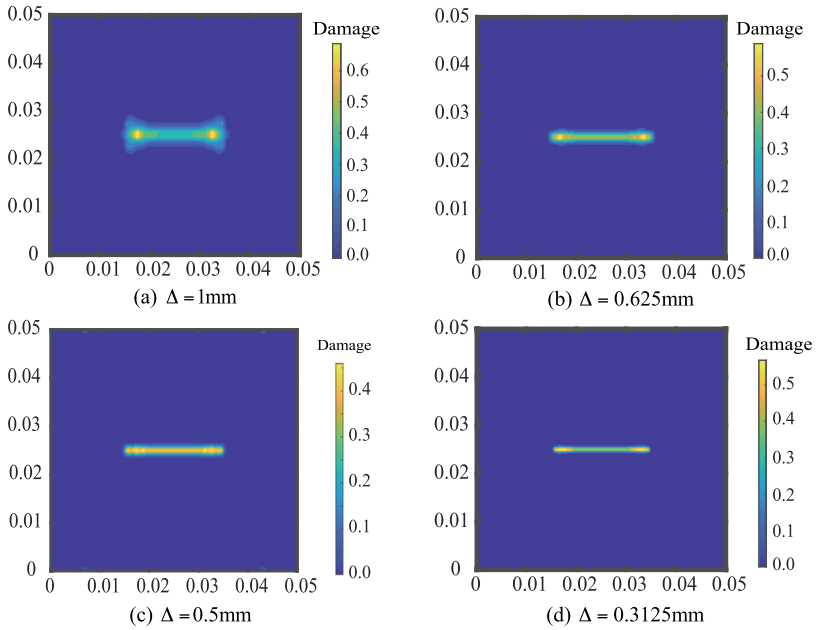

Fig. 16. Damage value with different discretization size.

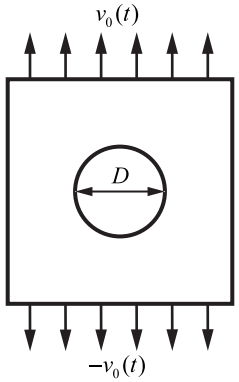

Fig. 17. Plate with a circular cutout.

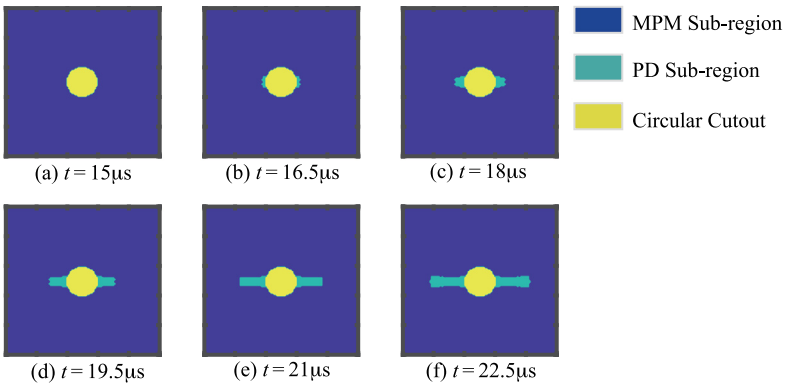

Fig. 18. Simulation sub-region of different time.

the particles. Under this situation, Eq. (32) is used to model the crack initiation of the continuum body with $\alpha = 0.95$ and $\sigma_{\max} = 400$ MPa.

The evolution of dynamic crack growth is observed when the stretch wave arrives the edge of the circular cutout. The partitions of the plate at different times are shown in Fig. 18. The proportion of PD particles as a function of time is plotted in Fig. 19.(a), and the crack growth distance as a function of time is shown in Fig. 19(b). The nodal value of damage at $t = 22.5$ μs is shown in Fig. 20. As shown in Fig. 18(b), the initial PD sub-region appears at two horizontal end of the circular cutout at $t = 16.5$ μs, because of the stress concentration. After that, the local damage value of some particles exceeds $\phi_0 = 0.38$ resulting in self-similar crack growth. The crack continues to propagate toward the external vertical boundaries, as shown in Figs. 18(c), (d), (e) and (f). As Fig. 19(b) shows, the maximum predicted crack growth speed is about 1750 m/s, which is less than the material Rayleigh wave speed of $v_r = 2800$ m/s. The crack growth speed is faster than the crack growth speed in Fig.19, because the mixed mode crack grows faster than the mode-I crack.

5.4. Kalthoff–Winkler experiment

Kalthoff Winkler Experiment [44–46] is a classical benchmark for dynamic crack growth simulation. As shown in Fig. 21, a rectangular steel plate with two parallel preset cracks is stricken by a steel impactor. The setup is depicted in Fig. 21. The thickness of the specimen is 0.01 m. The material density is 7800 kg/m^3, Young's modulus and Poisson's ratios are respectively 190 Gpa and 1/3, and the critical energy release rate is $G_0 = 6.9 \times 10^4$ J/m^2. The impact loading is imposed by applying an initial velocity of $v_0 = 22$ m/s to the first three layers of particles in the domain (see Fig. 21), and all other boundaries are free. In this simulation, the square plate is discretized into

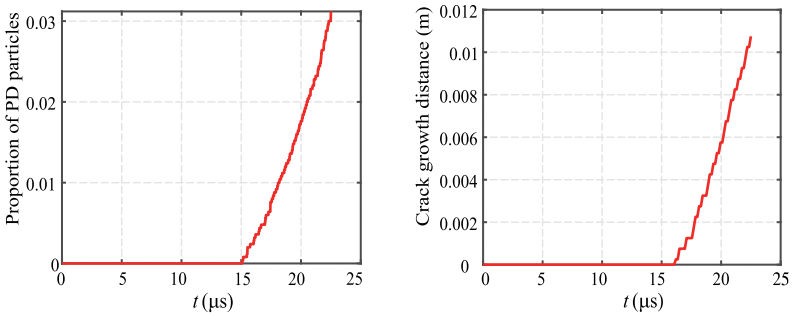

(a) Proportion of PD particles (b) Crack growth distance

Fig. 19. Proportion of PD particles and crack growth distance.

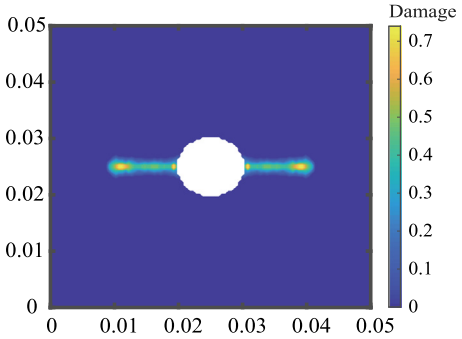

Fig. 20. Damage value at $t = 22.5$ μs.

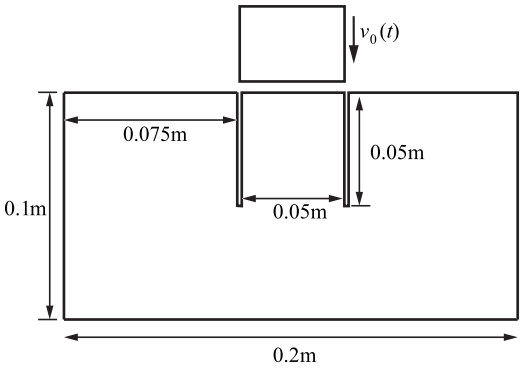

Fig. 21. Kalthoff–Winkler's experimental setup.

a set of particles with spacing $\Delta = 1$ mm, and horizon $\delta = 3.015\Delta$. The side length of the background grid cell is chosen as 0.1 mm, and the time step is set as $\Delta t = 5 \times 10^{-8}$ s. The particles are initially classified into MPM particles and PD particles based on Eq. (28). The initial partition of the plate is shown in Fig. 22(a), and the area near the pre-existing crack is set as PD subregion to simulate the discontinuity.

As shown in Fig. 22(c), the crack starts to grow around 25 μs. The initial crack tip speed is about 75% of the Rayleigh wave speed. As shown in Fig. 23, the angle of the crack propagation with respect to the original crack direction is about 63.0°, which matches with the observed angle of 70° for relatively low speed impact in the experiment [45,46]. As shown in Fig. 24, the damage of the plate can be divided into five stages: (1) $0 \sim 10.0$ μs: the number of PD particles remains unchanged; (2) $10.0 \sim 11.0$ μs: the proportion of PD particles raises to 3.0%

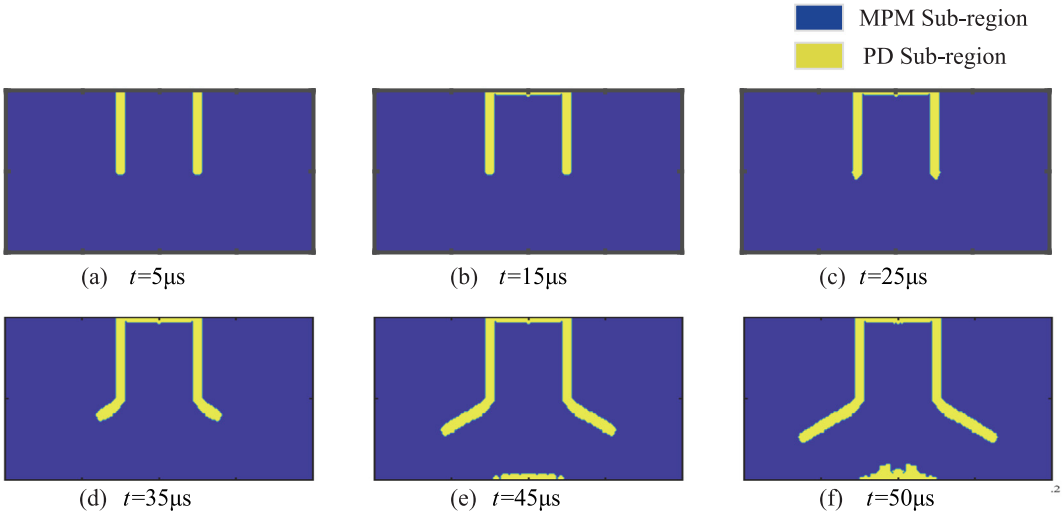

Fig. 22. Simulation sub-region of different time.

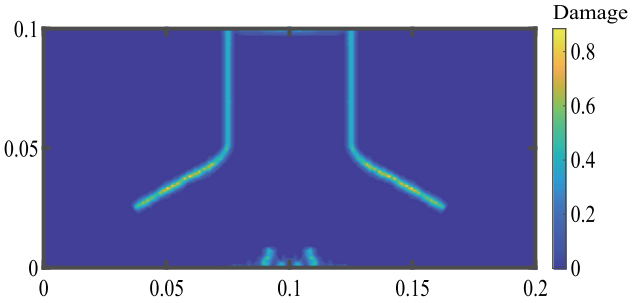

Fig. 23. Damage value at $t = 50$ μs.

with the damage of the top edge due to the apply of velocity boundary; (3) 11.0 $\sim$ 23.1 μs: the number of PD particles remains unchanged; (4) 23.1 $\sim$ 42.5 μs: the proportion of PD particles raises proportionally to 5.0% with the growth of the crack; (5) 42.5 $\sim$ 50.0 μs: the proportion of PD particles sharply raises compared to stage 4, because the stress wave reaches the bottom edge and the MPM particles are in tensile and converted to PD particles based on the stress criterion Eq. (32).

5.5. *Efficiency*

To investigate the efficiency of the adaptive PD/MPM algorithm, the improvement of the simulation efficiency is defined by

$$t_r = \frac{t_{\text{adaptive}} - t_{\text{PD}}}{t_{\text{PD}}}, \tag{51}$$

where t_{adaptive} and t_{PD} are the simulation time of adaptive PD/MPM method and PD, respectively. All examples in this paper are performed, and a PC with one Intel(R) core(TM) i9-9900K CPU @ 3.60 GHz is used.

As shown in Table 1, the simulation efficiency raises about 1/3 by the use of APDMPM. However, the examples in this paper cannot fully show the simulation efficiency of the APDMPM, because we just consider the elastic

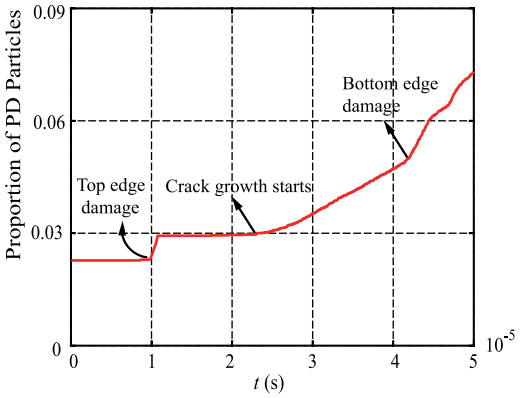

Fig. 24. Proportion of PD particles.

Table 1
Comparison in efficiency for different numerical examples.

	Plate with a Pre-existing Crack	Plate with a Circular Cutout	Kalthoff–Winkler Experiment
t_{adaptive}(s)	1.5099×10^3	2.2394×10^3	3.0951×10^3
t_{PD} (s)	2.4004×10^3	3.4031×10^3	4.5710×10^3
t_r	37.1%	34.2%	32.3%

materials here. In the simulation of plasticity with PD [29], the calculation of the interaction force between plastic PD particles will cost much more CPU time, and the APDMPM would show more efficiency improvement.

6. Conclusion

In this paper, an adaptive coupling approach of PD and MPM is proposed to fully take advantages of both the MPM and PD. A continuum body is partitioned into MPM, PD and hand-shake subregions. The failure region is modeled by the PD, while the remaining region is modeled by the MPM. The hand-shake region is employed to couple the MPM and PD. The MPM particles in the hand-shake subregion are located within the horizon of the PD particles, and the pairwise force between the MPM particles and the PD particles are imposed as the external force of the MPM particles. During the simulation, the MPM particles are converted to the PD particles adaptively with the extension of the failure part. Two adaptive conversion criteria are proposed related to the connection status and the stress status of the MPM particles, respectively.

To test the adaptive peridynamics material point method, four numerical examples are studied, including the spallation of a one-dimensional bar, a mode-I fracture propagation problem of a plate with a pre-existing crack, a mixed mode crack initiation problem, and the Kalthoff–Winkler's experiment. The numerical results show that the proposed adaptive peridynamics material point method has the capacity of modeling the crack initiation and propagation problems with both accuracy and efficiency.

Declaration of competing interest

The authors declare that they have no known competing financial interests or personal relationships that could have appeared to influence the work reported in this paper.

References

[1] T. Anderson, Fracture Mechanics: Fundamentals and Applications, CRC, 2005.
[2] Y. Chen, M. Wilkins, Numerical analysis of dynamic crack problems, Mech. Fract. 4 (1977) 295–345.
[3] N. Mos, J. Dolbow, T. Belytschko, A finite element method for crack growth without remeshing, Internat. J. Numer. Methods Engrg. 46 (1999) 131–150.
[4] X.P. Xu, A. Needleman, Numerical simulations of dynamic interfacial crack growth allowing for crack growth away from the bond line, Int. J. Fract. 74 (3) (1996) 253–275.

[5] A. Carpinteri, G. Ferro, G. Ventura, An augmented Lagrangian element-free (ALEF) approach for crack discontinuities, Comput. Methods Appl. Mech. Engrg. 191 (8–10) (2001) 941–957.
[6] P. Krysl, T. Belytschko, The element free Galerkin method for dynamic propagation of arbitrary 3-D cracks, Internat. J. Numer. Methods Engrg. 44 (1999).
[7] B.N. Rao, S. Rahman, Mesh-free analysis of cracks in isotropic functionally graded materials, Eng. Fract. Mech. 70 (1) (2003) 1–27.
[8] T. Rabczuk, T. Belytschko, Cracking particles: a simplified meshfree method for arbitrary evolving cracks, Internat. J. Numer. Methods Engrg. 61 (13) (2004) 2316–2343.
[9] T. Rabczuk, G. Zi, S. Bordas, H. Nguyen-Xuan, A simple and robust three-dimensional cracking-particle method without enrichment, Comput. Methods Appl. Mech. Engrg. 199 (37–40) (2010) 2437–2455.
[10] J.A. Nairn, Material point method calculations with explicit cracks, Comput. Model. Eng. Sci. 4 (6) (2003) 649–664.
[11] B. Wang, V. Karuppiah, H. Lu, R. Komanduri, S. Roy, Two-dimensional mixed mode crack simulation using the material point method, Mech. Compos. Mater. Struct. 12 (6) (2005) 14.
[12] Z. Chen, R. Feng, X. Xin, L. Shen, A computational model for impact failure with shear-induced dilatancy, Internat. J. Numer. Methods Engrg. 56 (14) (2010) 1979–1997.
[13] P. Yang, L. Yan, Z. Xiong, Z. Xu, Y. Zhao, Simulation of fragmentation with material point method based on gurson model and random failure, Comput. Model. Eng. Sci. 85 (3) (2012) 207–237.
[14] P. Yang, Y. Gan, X. Zhang, Z. Chen, W. Qi, P. Liu, Improved decohesion modeling with the material point method for simulating crack evolution, Int. J. Fract. 186 (1–2) (2014) 177–184.
[15] Y. Liang, T. Benedek, Y. Liu, X. Zhang, Material point method with enriched shape function for crack problems, Comput. Methods Appl. Mech. Engrg. 322 (Aug.1) (2017) 541–562.
[16] Y. Liang, X. Zhang, Y. Liu, Extended material point method for the 3D crack problems, Internat. J. Numer. Methods Engrg. (2021).
[17] K. Soga, E. Alonso, A. Yerro, K. Kumar, S. Bandara, Trends in large-deformation analysis of landslide mass movements with particular emphasis on the material point method, Geotechnique 66 (3) (2016) 248–273.
[18] Y. Cheon, H. Kim, An adaptive material point method coupled with a phase-field fracture model for brittle materials, Internat. J. Numer. Methods Engrg. 120 (8) (2019) 987–1010.
[19] S.A. Silling, M. Zimmermann, R. Abeyaratne, Deformation of a peridynamic bar, J. Elasticity 73 (1) (2003) 173–190.
[20] S.A. Silling, Reformulation of elasticity theory for discontinuities and long-range forces, J. Mech. Phys. Solids 48 (1) (2000) 175–209.
[21] S.A. Silling, E. Askari, A meshfree method based on the peridynamic model of solid mechanics, Comput. Struct. 83 (2005).
[22] S.A. Silling, M. Epton, O. Weckner, J. Xu, E. Askari, Peridynamic states and constitutive modeling, J. Elasticity 88 (2) (2007) 151–184.
[23] J.T. Foster, S.A. Silling, W.W. Chen, Viscoplasticity using peridynamics, Internat. J. Numer. Methods Engrg. 81 (10) (2010) 1242–1258.
[24] J. Amani, E. Oterkus, P. Areias, G. Zi, T. Nguyen-Thoi, A non-ordinary state-based peridynamics formulation for thermoplastic fracture, Int. J. Impact Eng. 87 (2016) 83–94.
[25] W. Hu, Y.D. Ha, F. Bobaru, Peridynamic model for dynamic fracture in unidirectional fiber-reinforced composites, Comput. Methods Appl. Mech. Engrg. 217–220 (Apr.1) (2012) 247–261.
[26] E. Madenci, M. Dorduncu, X. Gu, Peridynamic least squares minimization, Comput. Methods Appl. Mech. Engrg. 348 (2019) 846–874.
[27] S.A. Silling, M.L. Parks, J.R. Kamm, O. Weckner, M. Rassaian, Modeling shockwaves and impact phenomena with Eulerian peridynamics, Int. J. Impact Eng. 107 (Sep.) (2017) 47–57.
[28] H. Zhang, P. Qiao, A coupled peridynamic strength and fracture criterion for open-hole failure analysis of plates under tensile load, Eng. Fract. Mech. 204 (2018) 103–118.
[29] E. Madenci, S. Oterkus, Ordinary state-based peridynamics for plastic deformation according to von mises yield criteria with isotropic hardening, J. Mech. Phys. Solids 86 (2016) 192–219.
[30] D. Yang, X. He, J. Zhu, Z. Bie, A novel damage model in the peridynamics-based cohesive zone method (PD-CZM) for mixed mode fracture with its implicit implementation, Comput. Methods Appl. Mech. Engrg. 377 (2021) 113721.
[31] D. Yang, X. He, Y. Liu, A peridynamics-based cohesive zone model (PD-CZM) for predicting cohesive crack propagation, Int. J. Mech. Sci. 184 (2020) 105830.
[32] W. Liu, J.W. Hong, A coupling approach of discretized peridynamics with finite element method, Comput. Methods Appl. Mech. Engrg. 245–246 (OCT.15) (2012) 163–175.
[33] R.A. Wildman, G.A. Gazonas, A finite difference-augmented peridynamics method for reducing wave dispersion, Int. J. Fract. 190 (1–2) (2014) 39–52.
[34] P. Areias, D. Dias-Da-Costa, J.M. Sargado, T. Rabczuk, Element-wise algorithm for modeling ductile fracture with the rousselier yield function, Comput. Mech. 52 (6) (2013) 1429–1443.
[35] P. Areias, T. Rabczuk, P.P. Camanho, Finite strain fracture of 2D problems with injected anisotropic softening elements, Theor. Appl. Fract. Mech. 72 (2014) 50–63.
[36] G. Lubineau, Y. Azdoud, F. Han, C. Rey, A. Askari, A morphing strategy to couple non-local to local continuum mechanics, J. Mech. Phys. Solids 60 (6) (2012) 1088–1102.
[37] D. Sulsky, Z. Chen, H.L. Schreyer, Particle method for history-dependent materials., Comput. Methods Appl. Mech. Engrg. 118 (1–2) (1994) 179–196.
[38] X. Zhang, Z. Chen, Y. Liu, The Material Point Method: A Continuum-Based Particle Method for Extreme Loading Cases, Academic Press, 2016.
[39] F. Harlow, A Machine Calculation Method for Hydrodynamic Problems, Tech. Rep. LAMS-1956, Los Alamos Scientific Laboratory, 1955.
[40] Z. Zeng, Y.C. Su, X. Zhang, Z. Chen, Combining peridynamics and generalized interpolation material point method via volume modification for simulating transient responses, Comput. Part. Mech. 8 (2021) 337–347.

[41] Y. Lyu, J. Zhang, A. Sarafopoulos, J. Chang, J. Zhang, Integral-Based Material Point Method and Peridynamics Model for Animating Elastoplastic Material, Transactions on Computational Science, 2020.
[42] R. Ni, X. Zhang, A precise critical time step formula for the explicit material point method, Internat. J. Numer. Methods Engrg. 121 (2020) 4989–5016.
[43] H. Elizabeth, The moving griffith crack, Lond. Edinb. Dublin Philos. Mag. J. Sci. 42 (330) (1951) 739–750.
[44] X.P. Xu, A. Needleman, Numerical simulations of fast crack growth in brittle solids, J. Mech. Phys. Solids 42 (9) (1994) 1397–1434.
[45] J. Kalthoff, Modes of dynamic shear failure in solids, Int. J. Fract. 101 (2000) 1–31.
[46] J.F. Kalthoff, S. Winkler, Failure mode transition at high rates of shear loading, in: C.Y. Chiem, H.D. Kunze, L.W. Meyer (Eds.), Impact Loading and Dynamic Behavior of Materials, Vol. 1, 1987, pp. 185–195.